

Aerosol optical depth under “clear” sky conditions derived from sea surface reflection of lidar signals

MIN HE,^{1,*} YONGXIANG HU,² JIAN PING HUANG,³ AND KNUT STAMNES¹

¹Stevens Institute of Technology, Hoboken, NJ 07030, USA

²NASA Langley Research Center Hampton, VA 23681, USA

³Key Laboratory for Semi-Arid Climate Change of the Ministry of Education, College of Atmospheric Sciences, Lanzhou University, Lanzhou, 730000, China

*mhe1@stevens.edu

Abstract: There are considerable demands for accurate atmospheric correction of satellite observations of the sea surface or subsurface signal. Surface and sub-surface reflection under “clear” atmospheric conditions can be used to study atmospheric correction for the simplest possible situation. Here “clear” sky means a cloud-free atmosphere with sufficiently small aerosol particles. The “clear” aerosol concept is defined according to the spectral dependence of the scattering cross section on particle size. A 5-year combined CALIPSO and AMSR-E data set was used to derive the aerosol optical depth (AOD) from the lidar signal reflected from the sea surface. Compared with the traditional lidar-retrieved AOD, which relies on lidar backscattering measurements and an assumed lidar ratio, the AOD retrieved through the surface reflectance method depends on both scattering and absorption because it is based on two-way attenuation of the lidar signal transmitted to and then reflected from the surface. The results show that the clear sky AOD derived from the surface signal agrees with the clear sky AOD available in the CALIPSO level 2 database in the westerly wind belt located in the southern hemisphere, but yields significantly higher aerosol loadings in the tropics and in the northern hemisphere.

© 2016 Optical Society of America

OCIS codes: (010.0010) Atmospheric and oceanic optics ; (010.1110) Aerosols; (010.1285) Atmospheric correction; (010.1320) Atmospheric transmittance; (010.3640) Lidar; (010.4450) Oceanic optics.

References and links

1. T. Harmel and M. Chami, “Influence of polarimetric satellite data measured in the visible region on aerosol detection and on the performance of atmospheric correction procedure over open ocean waters,” *Opt. Express* **19**, 20960–20983 (2011).
2. H. R. Gordon and M. Wang, “Retrieval of water-leaving radiance and aerosol optical thickness over the oceans with SeaWiFS: a preliminary algorithm,” *Appl. Opt.* **33**(3), 443–452 (1994).
3. F. Steinmetz, P. Y. Deschamps, and D. Ramon, “Atmospheric correction in presence of sun glint: application to MERIS,” *Opt. Express* **19**(10), 9783–9800 (2011).
4. A. Prieto-Blanco, P. R. J. North, M. J. Barnsley, and N. Fox, “Satellite-driven modelling of Net Primary Productivity (NPP): Theoretical analysis,” *Remote Sens. Environ.* **113**(1), 137–147 (2009).
5. Y. Hu, K. Stamnes, M. Vaughan, J. Pelon, C. Weimer, D. Wu, M. Cisewski, W. Sun, P. Yang, B. Lin, A. Omar, D. Flittner, C. Hostetler, C. Trepte, D. Winker, G. Gibson, and M. Santa-Maria, “Sea surface wind speed estimation from space-based lidar measurements,” *Atmos. Chem. Phys.* **8**(13), 3593–3601 (2008).
6. H. Moosmüller, R. K. Chakrabarty, and W. P. Arnott, “Aerosol light absorption and its measurement: A review,” *J. Quant. Spect. Radiat. Transf.* **110**(10), 844–878 (2009).
7. M. Chin, R. A. Kahn, L. A. Remer, H. Yu, D. Rind, and G. Feigold, “Atmospheric aerosol properties and climate impacts,” U.S. Climate Change Science Program Synthesis and Assessment Product, (2009).
8. F. G. Fernald, B. M. Herman, and J. A. Reagan, “Determination of Aerosol Height Distributions by Lidar,” *J. Appl. Meteorol.* **11**(3), 482–489 (1972).
9. A. H. Omar, D. M. Winker, M. A. Vaughan, Y. Hu, C. R. Trepte, R. A. Ferrare, K.-P. Lee, C. A. Hostetler, C. Kittaka, R. R. Rogers, R. E. Kuehn, and Z. Liu, “The CALIPSO Automated Aerosol Classification and Lidar Ratio Selection Algorithm,” *J. Atmos. Oceanic Technol.* **26**(10), 1994–2014 (2009).
10. A. H. Omar, D. Winker, and J. Won, “Aerosol models for the CALIPSO lidar inversion algorithms,” *Proc. SPIE* **5240**, 153–164 (2004).

11. W. Junkermann and J. M. Hacker, "Ultrafine particles over Eastern Australia: an airborne survey," *Tellus B*, **67**, 25308 (2015).
12. W. Junkermann, B. Vogel, and M. Bangert, "Ultrafine particles over Germany - an aerial survey," *Tellus B*, **68**, 29250 (2016)
13. G. L. Schuster, M. Vaughan, D. MacDonnell, W. Su, D. Winker, O. Dubovik, T. Lapyonok, and C. Trepte, "Comparison of calipso aerosol optical depth retrievals to aeronet measurements, and a climatology for the lidar ratio of dust," *Atmos. Chem. Phys.* **12**, 11641–11697 (2012).
14. T. J. Thorsen and Q. Fu, "Calipso-inferred aerosol direct radiative effects: Bias estimates using ground-based raman lidars," *J. Geophys. Res.: Atm.* **120**(23), 12209–12220 (2015).
15. B. R. Bzdek, M. R. Pennington and M. V. Johnston, "Single particle chemical analysis of ambient ultrafine aerosol: A review," *Journal of Aerosol Science* **52**, 109–120 (2012).
16. W. A. Hoppel, G. M. Frick, and J. W. Fitzgerald, "Surface source function for sea-salt aerosol and aerosol dry deposition to the ocean surface," *J. Geophys. Res.: Atm.* **107**(D19), 2156–2202 (2002).
17. D. Josset, J. Pelon, A. Protat, and C. Flamant, "New approach to determine aerosol optical depth from combined CALIPSO and CloudSat ocean surface echoes," *Geophys. Res. Lett.* **35**(10), L10805 (2008)
18. D. Josset, "Determination of aerosol optical properties using ocean reflectance," *SPIE Newsroom*, 2–4. (2009)
19. S. A. Ackerman, K. I. Strabala, W. P. Menzel, R. A. Frey, and C. C. Moeller, L. E. Gumley, "Discriminating clear sky from clouds with modis," *J. Geophys. Res.* **103**(D24), 32–141 (1998).
20. R. W. Saunders and K. T. Kriebel, "An improved method for detecting clear sky and cloudy radiances from avhrr data," *Int. J. of Remote Sensing* **9**(1), 123–150 (1988).
21. C. Cox and W. Munk, "Measurement of the Roughness of the Sea Surface from Photographs of the Sun's Glitter," *J. Opt. Soc. Am.* **44**(11), 838 (1954).
22. W. Wiscombe, "Improved Mie scattering algorithms," *Appl. Opt.* **19**, 1505–1509 (1980).
23. D. M. Winker, M. A. Vaughan, A. Omar, Y. Hu, K. A. Powell, Z. Liu, W. H. Hunt, and S. A. Young, "Overview of the CALIPSO mission and CALIOP data processing algorithms," *J. Atmos. Oceanic Technol.* **26**(11), 2310–2323 (2009).
24. C. Hostetler, Z. Liu, and J. Reagan, "CALIOP Algorithm Theoretical Basis Document Calibration and Level 1 Data Products," NASA Langley Research Center Document PC-SCI-201 (April) (2006).
25. P. Hwang, "Foam and roughness effects on passive microwave remote sensing of the ocean," *IEEE Trans. Geosci. Remote Sens.* **50**(8), 2978–2985 2012
26. D. B. Ross and V. Cardone, "Observations of oceanic whitecaps and their relation to remote measurements of surface wind speed," *J. Geophys. Res.* **79**(3), 444–452 (1974).
27. X. Lu, Y. Hu, C. Trepte, S. Zeng, and J. H. Churnside, "Ocean subsurface studies with the calipso spaceborne lidar," *J. Geophys. Res. Oceans* **119**(7), 4305–4317 (2014)
28. S. R. Massel, *Ocean Waves Breaking and Marine Aerosol Fluxes* (Springer, 2007)
29. Y. Hu, Z. Liu, D. Winker, M. Vaughan, V. Noel, L. Bissonnette, G. Roy, and M. McGill, "Simple relation between lidar multiple scattering and depolarization for water clouds," *Opt. Lett.* **31**(12), 1809–1811 (2006).
30. Y. Hu, "Depolarization ratio-effective lidar ratio relation: Theoretical basis for space lidar cloud phase discrimination," *Geophys. Res. Lett.* **34**(11), 1–4 (2007).
31. F. Wentz and T. Meissner, "Algorithm theoretical basis document (atbd) amsr ocean algorithm (version 2)," RSS Tech. Proposal 121599A-1, Remote Sensing Systems, Santa Rosa, CA. On-line document available at: <http://www.ssmi.com/tmiInfo.html>. (2000).
32. Y. Hu, M. Vaughan, Z. Liu, B. Lin, P. Yang, D. Flittner, B. Hunt, R. Kuehn, J. Huang, D. Wu, S. Rodier, K. Powell, C. Trepte, and D. Winker, "The depolarization - attenuated backscatter relation: CALIPSO lidar measurements vs. theory," *Opt. Express* **15**(9), 5327–5332 (2007).
33. Y. Hu, D. Winker, M. Vaughan, B. Lin, A. Omar, C. Trepte, D. Flittner, P. Yang, S. L. Nasiri, B. Baum, R. Holz, W. Sun, Z. Liu, Z. Wang, S. Young, K. Stamnes, J. Huang, and R. Kuehn, "CALIPSO/CALIOP cloud phase discrimination algorithm," *J. Atmos. Oceanic Technol.* **26**(11), 2293–2309 (2009).
34. K. Stamnes and J. J. Stamnes, *Radiative Transfer in Coupled Environmental Systems: An Introduction to Forward and Inverse Modeling* (Wiley-VCH, 2015).
35. A. Bucholtz, "Rayleigh-scattering calculations for the terrestrial atmosphere," *Appl. Opt.* **34**(15), 2765–2773 (1995).
36. R. B. Miles, W. R. Lempert, and J. N. Forkey, "Laser rayleigh scattering," *Meas. Sci. Technol.* **12**(5), R33 (2001)
37. B. van Ginneken, M. Stavridi, and J. J. Koenderink, "Diffuse and specular reflectance from rough surfaces," *Appl. Opt.* **37**(1), 130–139 (1998).
38. D. Barrick, "Rough surface scattering based on the specular point theory," *IEEE Trans. Antennas Propag.* **16**(4), 449–454 (1968).
39. J. Wu, "Mean square slopes of the wind-disturbed water surface, their magnitude, directionality, and composition," *Radio Science* **25**(1), 37–48 (1990).
40. A. H. Monahan, "The Probability Distribution of Sea Surface Wind Speeds. Part I: Theory and SeaWinds Observations," *J. clim.* **19**(24), 497–520 (2006).
41. T. Shi and N. Cressie, "Global statistical analysis of misr aerosol data: a massive data product from nasa's terra satellite," *Environmetrics* **18**(7), 665–680 (2007).
42. J. Huang, P. Minnis, B. Chen, Z. Huang, Z. Liu, Q. Zhao, Y. Yi, and J. K. Ayers, "Long-range transport and

- vertical structure of Asian dust from CALIPSO and surface measurements during PACDEX,” *J. Geophys. Res.:Atm.* **113**(D23), 1–13 (2008).
43. J. Huang, T. Wang, W. Wang, Z. Li, and H. Yan, “Climate effects of dust aerosols over east asian arid and semiarid regions,” *J. Geophys. Res.: Atm.* **119**(19), 11398–11416 (2014).

1. Introduction

Besides the impact of aerosols on climate, which has been extensively studied, atmospheric correction of satellite observations is needed to retrieve accurate information about the Earth’s surface. Aerosols constitute an important and variable optically-significant component that affects light propagation between the satellite and the surface. Accurate atmospheric correction is needed to obtain reliable water-leaving radiances [1–3] used to study ocean productivity [4], and to derive accurate values of sea surface wind speed from satellite data [5].

In principle, there are several ways to estimate the aerosol optical depth. Current aerosol measuring methods, including *in situ* observations, ground-based network observations and satellite observations, complement each other. The AODs provided by these measurement types have sufficiently large differences that assimilation between them must be done by modeling. Moosmuller et al. [6] discussed the challenges encountered in measurements of aerosol absorption.

Satellite measurements provide the only way to obtain aerosol information synchronous to surface measurements on a global scale. Passive satellite remote sensing relies on assumptions about the particle size distribution and composition and is not sensitive to particles smaller than about $0.1\ \mu\text{m}$ [7]. Being an active sensor, the Cloud-Aerosol Lidar with Orthogonal Polarization (CALIOP) is one of the payloads deployed on the Cloud-Aerosol Lidar and Infrared Pathfinder Satellite Observation (CALIPSO) satellite. Retrieval of extinction profiles from lidar observations is based on knowledge of the lidar ratio and the target backscatter [8]. The lidar ratio depends on the aerosol composition as well as size and shape distributions which have large spatial and temporal variability. Thus the retrieval of AOD relies on the aerosol classification and a lidar ratio assumed to be known according to aerosol type [9]. Aerosol models are established based on AERONET observations [10]. In principle, accurate retrieval of aerosol absorption from elastic backscatter lidar measurements is difficult using the traditional method. Due to the vertical resolution and the signal being contaminated by strong surface backscatter, CALIOP has limited ability to observe aerosols near the surface where most of the aerosol particles are located. Based on aircraft observations, Junkermann et al. [11, 12] showed that the major source of fine particles is in the boundary layer. Schuster et al. [13] showed that the AOD products of CALIOP and AERONET have significant differences for strongly absorbing dust aerosols. Comparing aerosol observations obtained from CALIOP and from ground-based Raman lidar data, Thorsen and Fu [14] found that CALIOP has limited ability to detect aerosols having a significant direct radiative effect defined as the change in irradiance by the aerosol loading. This problem can result in a 30-50% underestimation of the aerosol direct radiative effect.

As discussed above, current satellite-based lidar aerosol retrieval algorithms have limited ability to evaluate radiative impact from aerosols with small optical depths. However, this aerosol population plays an important role in cloud nucleation processes and atmospheric correction of surface properties, and it affects human health. Optically, the concept of small particles refers to particles with size smaller than the wavelength of the incident light. The aerosol particle size ranges from a few nanometers (the size of a molecular cluster) to a few tens of micrometers [7]. According to the size, the particles are divided into ultrafine particles (diameter smaller than $100\ \text{nm}$), fine particles (diameter range $100\ \text{nm} - 2.5\ \mu\text{m}$) and coarse particles (diameter larger than $2.5\ \mu\text{m}$). Most of the current *in situ* aerosol observations do not include the ultrafine particles, although particles on the small side of the size distribution have attracted the interest of several investigators. Bzdek et al. [15] summarized several methods that can measure the properties of

ultrafine particles *in situ*. Airborne observations of the ultrafine particle population were made in the coastal area of Eastern Australia [11] and in Germany [12].

The aerosol residence time is typically one week or less [7]. Considering dry deposition processes, including gravitational settling, Brownian diffusion, and turbulent deposition, the deposition velocity was found to decrease with decreasing particle size from 100 μm , and having a minimum for sizes in the range between 0.1 and 1 μm [16]. Thus, particles in this size range [0.1 – 1 μm] appear to have the longest atmospheric residence time, and may reach a steady-state in which source equals loss.

In this paper, based on Rayleigh scattering theory, we define particles that have the strongest spectral dependence of the backscatter as small particles. These small particles should include the optically-significant portion of the ultrafine particles and a portion of the fine particles. Our goal is to investigate the optical depth of these small particles over the ocean on a global scale.

Based on CALIPSO observations of lidar signals reflected from the sea surface and collocated wind speed data provided by the AMSR-E program, the background aerosol optical depth for the cleanest sky conditions can be derived from the attenuation of the lidar signal. Josset et al. [17, 18] introduced the method of using surface reflectance to estimate the AOD. Josset et al. [17] used surface reflectance data obtained from CloudSat observations, and they compared AODs retrieved by the surface reflection method with MODIS observations. The AOD provided by the sea surface backscatter and surface wind speed method has a significant advantage [17, 18], because it is derived from atmospheric attenuation of the sea surface backscatter without any assumptions about the aerosol microphysical properties, and it includes absorption.

In this paper, we use combined CALIPSO and AMSR-E observations to estimate the AOD based on an estimation of atmospheric attenuation. We focus on “clear” sky conditions because remote sensing based on signals reflected from the surface can be done under selected sky conditions. The “clear” sky concept introduced in this paper is different from the conventional meaning which means a cloudless sky (see for example: [19] and [20]). Here we define a “clear” sky to mean a cloudless sky with aerosols consisting of small size particles with strong wavelength dependence.

The CALIOP instrument can provide attenuated backscatter profiles at two wavelengths, 532 nm and 1064 nm. The profile ranges from -2 km to 40 km. Here ‘-’ means below the sea surface. The profile has a vertical resolution of 30 m near the surface [-0.5 km to 8 km], decreasing to 300 m at an altitude of 30 km. Thus, we can get the surface signal and atmospheric information simultaneously. The summation of the backscatter between -300 and 30 m is defined to be the Integrated Surface Return (*ISR*) while the summation of the backscatter between 30 m and 30 km is defined to be the Integrated Atmosphere Return (*IAR*). The *ISR* is the surface reflected energy attenuated by the atmosphere. The *IAR* depends on the scattering and absorption (attenuation) ability of the atmosphere.

The surface reflection includes specular and diffuse components. When specular reflection occurs, the relatively weak diffuse reflection is usually ignored. The observing zenith angle was 0.3° for CALIPSO before September 2009, but it was changed to 3° thereafter. Specular reflection occurs when the local surface slope equals the observing zenith angle. For a wind-roughened sea surface, the slope distribution may be represented by a Gram-Charlier distribution [21]. The probability distribution of surface slopes is determined by the slope variance σ^2 , which is empirically related to the surface wind speed. Thus we can get an estimate of rough surface backscatter from the surface wind speed. The atmospheric attenuation can be estimated by comparison of the CALIOP observed *ISR* and the surface backscatter estimated from the wind speed provided by AMSR-E. At the CALIOP observation channels (532 nm and 1064 nm), for clear sky conditions, the effective attenuation is due to the bulk density of molecules (Rayleigh scattering), ozone absorption, and scattering and absorption by suspended particles (aerosols). Unlike the aerosols, the distribution of air molecules (diatomic oxygen and nitrogen) and ozone is

relatively steady both in time and space. The contribution due to Rayleigh (molecular) scattering and ozone absorption can be estimated from density profiles provided by the Global Modeling and Assimilation Office (GMAO) and integrated into the CALIPSO level 1 data set, and extinction coefficients can be calculated from theory. Thus we can get the AOD (including scattering and absorption) through the combined use of CALIPSO's *ISR* and the surface wind speed provided by AMSR-E.

The concept of "clear" sky can be precisely defined by the quantity *IAR* provided by CALIOP observations in the two channels. According to the Mie-Debye theory, (see for example, [22]), the scattering/extinction properties of particles can be calculated if we know the refractive index and the size parameter $x = \frac{2\pi a}{\lambda}$ where a is the radius of the particle (assumed to have spherical shape). When the size parameter $x < 5$, both the extinction and the scattering cross sections increase with x . Hence, the smaller particles are sensitive to shorter wavelengths and larger particles to longer wavelengths of light. The ratio of *IAR* values in the two CALIOP channels is an indicator of the particle size. We define this value as the Equivalent Color Ratio ($ECR = IAR_{1064}/IAR_{532}$). According to Mie theory, the scattering cross section of large particles has a weak dependence on wavelength, while small particles has a much larger scattering cross section in the 532 nm channel than in the 1064 nm channel. We introduce a method that can filter out the small but optically-significant particles based on satellite-based lidar observations. The global distribution of the AOD of these small particles is derived.

2. Data and method

We use the combined CALIOP *ISR* and AMSR-E wind speed products to estimate the AOD related to the attenuation of the surface signal based on reflection by the wind-roughened sea surface. The dataset is the night time part from September 2006 to September 2011. The CALIPSO satellite carrying the CALIOP instrument and the Aqua satellite carrying the AMSR-E instrument are both in the A-train constellation. They have the same flight orbit and the distance between them is about 80 seconds. The wind speed represents an average over a certain scale based on the sea surface roughness. We will assume that the properties of the observed target remain unchanged during 80 seconds. The characteristics and capabilities of CALIOP are described elsewhere [23]. The lidar equation is given by [24]

$$P(r, \lambda) = \frac{1}{r^2} E_0 G C \beta(r, \lambda) \exp[-2 \int_0^r \sigma(r', \lambda) dr'] \quad (1)$$

where r is the distance from satellite to target, and λ is the observation wavelength, which for CALIOP is either 532 nm or 1064 nm. $P(r, \lambda)$ is the measured signal (in unit of [J]). E_0 is the average laser energy for the single-shot or composite profile (in unit of [J]). G is the gain of the system, and C is the calibration constant. $\beta(r, \lambda)$ is the volume backscatter at r [km^{-1}], and $\sigma(r, \lambda)$ is the volume extinction coefficient [km^{-1}]. At 532 nm the extinction is due to molecular scattering, ozone absorption, and aerosol scattering and absorption. The contribution due to molecular scattering and ozone absorption can be ignored at 1064 nm. The attenuation part of the lidar equation can be approximated as:

$$T^2 = \exp[-2 \int_0^r \sigma(r', \lambda) dr'] \approx \exp(-2(\tau_o + \tau_m + \tau_a)) \quad (2)$$

where τ_o is the ozone optical depth, τ_m is the molecular scattering optical depth, and τ_a is the AOD due to scattering and absorption.

The CALIOP receiver with a digitization rate of 10 MHz has the ability to get backscatter signals from 75.3 km to -18.5 km. Here '-' means below the sea surface. The CALIOP team provides backscatter profiles ranging from 40 km to -2 km. This vertical range is divided into

583 bins with different vertical resolution due to the vertical change of the atmospheric density. From the top of the atmosphere (TOA) to the Earth's surface, the summation of attenuated backscatter between the 89th and the 560th bins gives the *IAR* and the summation of the attenuated backscatter between the 561st bin and the 572ed bin gives the *ISR*.

For the visible channel at 532 nm, the subsurface radiance transmitted through the water-air interface can also contribute to the reflectance. The areal coverage of whitecaps and foams increases with wind speed [25, 26]. However, contributions from the subsurface signal as well as from whitecaps and foams can be related to the depolarization ratio. Lu et al. [27] showed that the subsurface backscatter is linearly related to the depolarization ratio, while contributions from whitecaps and foams are due to multiple scattering effects [28], which are also related to the depolarization ratio as discussed by Hu et al. (2006, 2007) [29, 30]. In this paper, we use the method described by Hu et al. [5] to remove contributions from subsurface backscatter as well as from multiple scattering off whitecaps and foams to the reflectance by subtracting a certain percentage based on the depolarization ratio.

The AMSR-E wind speed product is described by Wentz et al. [31]. Based on comparisons with buoy measurements, the AMSR-E near surface wind speed product has an rms error of about 1 m/s [31]. The footprint of AMSR-E is 20 km (cross-track) while the footprint of CALIOP has a diameter of 70 m. The running averages are applied to the CALIOP data over 7 shots and 15 shots separately.

Figure 1 shows the relationship between the *IAR* and the AOD. According to the definition, the *IAR* is related to the backscatter and extinction. The exact relation between the *IAR* and AOD depends on the microphysical properties of the particles. The *IAR* is related to the AOD statistically with a correlation coefficient of 0.51 at a confidence interval of 95%. An increase in aerosol loading leads to an increase in the *IAR* value, and a threshold value of the *IAR* can be used to select small particle cases. We chose *IAR* values smaller than 0.015 [sr^{-1}] as the clear sky condition in this paper. This choice will exclude most large particles but include the small particles. As shown elsewhere [30, 32, 33] non-spherical ice particles can result in strong returns in the perpendicular channel. Therefore, a threshold of the depolarization ratio of 0.2 is also used to exclude cirrus cloud particles. Based on this selection rule, about 3% of the CALIPSO level 2 AOD values (532 nm channel) are smaller than 0.01 and 8% are smaller than 0.02.

As alluded to above, the Equivalent Color Ratio (*ECR*) concept is introduced to define the aerosol population:

$$ECR = \frac{IAR_{1064}}{IAR_{532}} \quad (3)$$

where 1064 and 532 refer to the two CALIOP channels. Figure 2 shows a histogram distribution of the *ECR*. The distribution can be regarded as a superposition of several normal distributions. The smallest one peaks at 0.22 while the others peak close to 1.0. The distributions peaking at 1.0 (or close to 1.0) are believed to be due to large particles. The distribution peaking at 0.22 is due to small particles including air molecules and small aerosol particles. Inserting the lidar equation (Eq. 1) into Eq. 3, we find that the *ECR* can be expressed as:

$$ECR = \frac{\sum_i \beta_i^{1064} \cdot \exp(-2\tau_i^{1064})}{\sum_i \beta_i^{532} \cdot \exp(-2\tau_i^{532})} \quad (4)$$

where i denotes the bin number in the CALIOP vertical profile ranging from 89 to 560, and τ_i is the total optical depth due to ozone absorption, molecules scattering, and aerosols absorption and scattering along the light path from the i th bin to the TOA. The inherent optical properties of molecules is described by electromagnetic scattering theory. For homogeneous spherical particles, Mie-Debye theory applies, which for small particles gives results applicable to molecules (see e.g. [34]). The volume scattering coefficient of molecular scattering by the Earth's atmosphere

can be expressed as [35]:

$$\sigma(\lambda) = \frac{24\pi^3(n_s^2 - 1)^2}{\lambda^4 N_s(n_s^2 + 2)^2} \cdot \frac{6 + 3\rho_n}{6 - 7\rho_n} \quad [\text{km}^{-1}] \quad (5)$$

where λ is the wavelength (in centimeters), n_s is the refractive index, N_s is the molecular number density [molecules m^{-3}], and ρ_n is the depolarization factor (0.02842 at 532 nm and 0.02730 at 1064 nm).

For the US 1966 standard atmosphere we have: $\sigma(532) = 1.336 \times 10^{-2} \text{ (km}^{-1}\text{)}$, $\sigma(1064) \approx 6.964 \times 10^{-4} \text{ (km}^{-1}\text{)}$ and the backscattering to scattering cross section ratio is $\frac{3}{8\pi}$ [36]. Hence, the backscattering cross section can be expressed as $\beta(\lambda) = \frac{3}{8\pi}\sigma(\lambda)$. The average molecular scattering optical depth is 0.11, and the average ozone absorption optical depth is 0.02 at 532 nm. The average is calculated based on the ozone and molecular density profiles available in the CALIPSO level 1 dataset. We obtain an estimated *ECR* ranging from 0.06 to 0.09 for a clear (cloud- and aerosol-free) atmosphere. However, from the distribution of the *ECR* observed by CALIOP, the smallest center of the *ECR* distribution is at 0.22 (see Fig. 2), which is twice that of the pure molecular (clear) atmosphere. We conclude that our “clear sky” atmosphere, consisting of molecules mixed with small size aerosol particles, has a stronger backscattering signal than a “pure” (cloud and aerosol-free) atmosphere.

A cloud-free atmosphere with a *IAR* threshold value of 0.015 and a *ECR* threshold value of 0.4 is defined as “clear” sky conditions (see Fig. 2). The data are selected before the running mean process to increase the signal-to-noise ratio. The maximum “run mean” range is 15 shots. Using this selection rule, we get more than 10 million valid shots of observations for our “clear sky” aerosol study. These dataset covers the ocean part of the Earth, but the polar regions are excluded due to its high percentage of sea ice coverage.

Focusing on the sea surface, and using Eq. 2, we find it convenient to introduce a normalized version of Eq. 1:

$$\gamma' = C\gamma \exp(-2(\tau_o + \tau_m + \tau_a)) \equiv C\gamma T^2 \quad (6)$$

where the distance r , the system gain G , and the transmitter energy E_0 have been absorbed in the normalization. In Eq. 6, γ' is the CALIOP received signal or the atmospheric attenuated sea surface backscattering signal, C is the calibration constant, and γ is the signal backscattered from the wind-roughened sea surface target. The two-way atmospheric transmittance $T^2 = \exp(-2(\tau_o + \tau_m + \tau_a))$ includes direct attenuation due to scattering and absorption, but ignores multiple scattering. During nighttime, the 532 nm channel is well calibrated by a comparison of the observed signal with the estimated signal due to molecular scattering from the upper atmospheric layers assumed to be cloud- and aerosol-free.

Empirically, the signal backscattered from the sea surface is given by $\gamma = \gamma_U$ and γ_U can be estimated from the near surface wind speed U and a surface reflection model (see Eq. 10 below). The two-way atmospheric transmittance can then be expressed as $T^2 = \frac{1}{C} \frac{\gamma'}{\gamma_U}$, where γ_U is the signal backscattered from the surface, which can be estimated from the near surface wind speed U according to the empirical relation provided by Hu et al. (2008) [5]. The CALIOP sensor is well calibrated during nighttime, especially in the 532 nm channel, implying that the calibration constant can be dropped. For the 532 nm channel, extinction is due to molecular scattering, ozone absorption, as well as aerosol scattering and absorption, while for the 1064 nm channel, extinction due to molecular scattering and ozone absorption is negligible and can be ignored. Hence, the AOD $\tau_{\lambda,a}$ can be expressed as:

$$\tau_{532,a} = -0.5 * \log\left(\frac{\gamma'_{532}}{\gamma_{U,532}}\right) - \tau_m - \tau_o \quad (7)$$

$$\tau_{1064,a} = -0.5 * \log\left(\frac{\gamma'_{1064}}{\gamma_{U,1064}}\right) \quad (8)$$

where τ_m is the optical depth due to molecular scattering and τ_o is the optical depth due to ozone absorption.

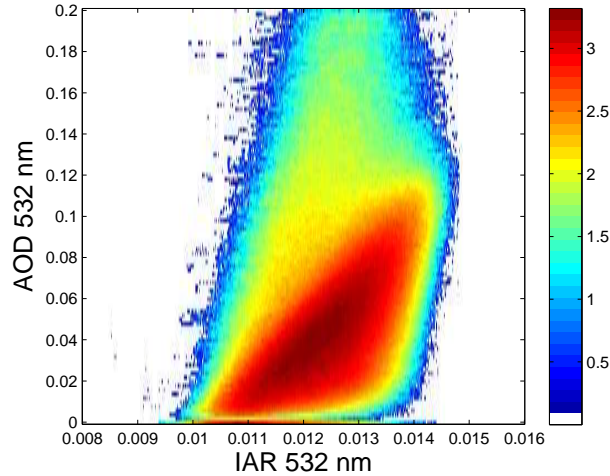


Fig. 1. Scatter plot of the Integrated Atmosphere Return (*IAR*, *x*-axis) and AOD (*y*-axis) at 532 nm. The colors are \log_{10} [number of occurrence]. The correlation coefficient between them is 0.51 on a 95% confidence interval.

3. The sea surface reflection model

The wind-roughened sea surface has both specular and diffuse reflection components. For small angles of incidence and observation, the shadowing effect can be ignored. Since CALIOP is an active sensing instrument, and the lidar equation is derived under the assumption that only single scattering is important, the diffuse part of the reflection is by assumption small compared with the specular part. Thus, the reflectance of the sea surface is determined primarily by the specular reflectance and the probability that the surface has a slope which makes the angles of incidence and observation coincide. Only for this geometry, will specular reflection occur. The reflectance of a calm water surface is simply determined by Fresnel's law if we ignore the contribution from subsurface scattering.

The reflection from a wind-roughened sea surface is determined by the Fresnel formula and the statistical distribution of the slopes of local facets of the sea surface. Usually, the facet slope distribution is assumed to be a one- or two-dimensional Gaussian distribution in two perpendicular (up-wind and cross-wind) directions [37]. If the slope variance is the same in the two directions, then the two-dimensional probability distribution collapses to a one-dimensional (isotropic) distribution, which can be expressed as (for details see e. g. [34]):

$$P(\tan \theta, \sigma) d \tan \theta = \frac{1}{\pi \sigma^2} \exp\left(-\frac{\tan^2 \theta}{\sigma^2}\right) d \tan \theta \quad (9)$$

where θ is the tilt of the surface facet with respect to the vertical. Only when the tilt is the same as the CALIOP angle of incidence θ_0 , will specular reflection occur. The probability that the facet has tilt θ_0 is determined by the variance of the distribution σ^2 .

Based on the specular reflection theory [38], the backscatter from a rough surface is caused by the slope distribution of small facets on the surface, which we assume can be represented by a Gaussian distribution. Based on the Gaussian probability distribution given by Eq. 9, the signal

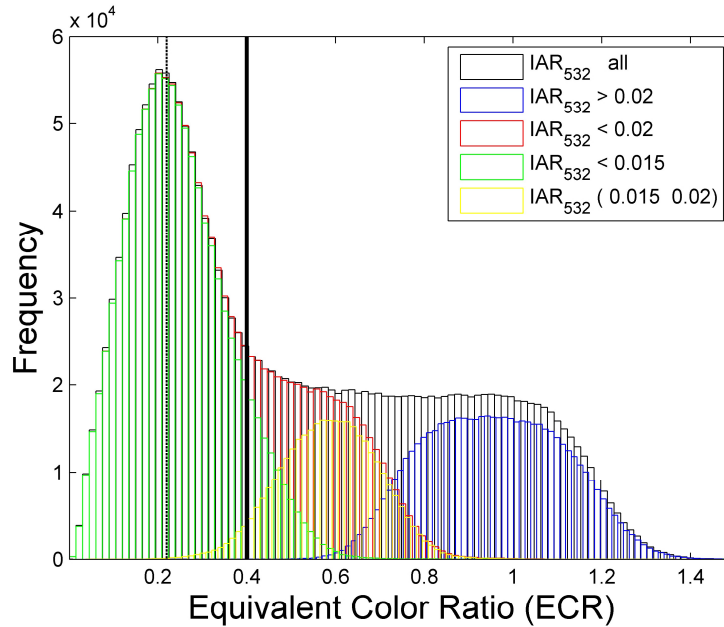


Fig. 2. Atmospheric equivalent color ratio (ECR) for nighttime observations. The cases used in this statistical study is the “clear” sky atmosphere (see text for definition). The y-axis represents the frequency of occurrence. The broken vertical line gives the location of the normal distribution with the smallest peak value of 0.22. The solid vertical line indicates the truncation at 0.4. The ECR distribution is a superposition of several normal distributions of different particle sizes. For IAR_{532} values larger than 0.02 (blue color), the ECR peaks close to 1. For IAR_{532} values in between 0.015 and 0.02 (yellow color), the ECR is centered at 0.6. If we select a IAR_{532} threshold of 0.015 (green color), most small particles with a small peak ECR value will be included. The unit of IAR_{532} is sr^{-1} .

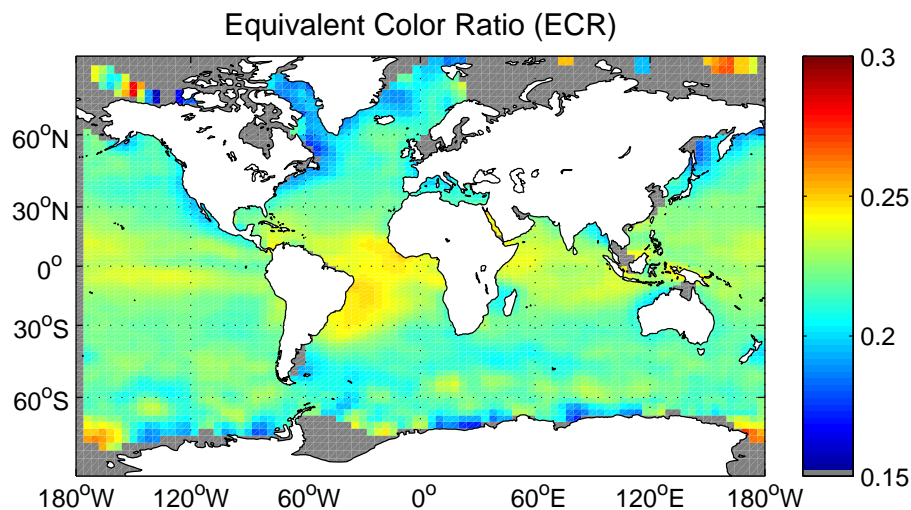


Fig. 3. The global distribution of the atmospheric Equivalent Color Ratio (ECR) of the selected “clear” sky conditions. The average is made on a 2° (latitude) by 4° (in longitude) grid box over the 5-year dataset.

backscattered from the sea surface can be expressed as [5]:

$$\gamma = \frac{\rho}{4\pi\sigma^2 \cos^4 \theta} \exp\left(-\frac{\tan^2 \theta}{\sigma^2}\right) \quad (10)$$

where ρ is the Fresnel reflectance of the sea surface. For the 532 nm wavelength, $\rho = 0.0209$ and for the 1064 nm wavelength, $\rho = 0.0193$. σ^2 is the variance of the surface slope distribution, and θ is the observation angle (in degree) of the lidar signal receiver. The observation angle in degrees was 0.3° (and 3° after Sep. 2009) for the dataset used in this study.

The slope variance σ^2 is empirically represented by the wind speed U . But σ^2 vs U relations obtained from three sources [5], [21] and [39] are slightly different. The frequently cited relation is the one provided by Cox and Munk [21], who obtained it based on the assumption that the surface slopes obey a two-dimensional Gram-Charlier distribution. The variance, skewness, and kurtosis were parameterized by wind speed at the height of 10 m. However, the uncertainty of the skewness and kurtosis obtained by Cox and Munk [21] is large, of the same or even higher order of magnitude as the parameterized coefficients. The normal distribution is true only when the probability of positive slope equals that of negative slope, implying that the slope distribution is close to Gaussian for wind speeds that are not too big and not too small. If the wind speed is small, the sea surface slope is in a developing stage, and the skewness and kurtosis are significant. If the wind speed is large, the change of the dominant force will destroy the Gaussian distribution. Some authors express the deviation from Gaussian distribution by using piece-wise functions of the σ^2 vs U relation [5, 39]. Hu et al. [5] explained that the piece-wise relation is needed because the dominant force is different for moderate and strong wind speeds.

Cox-Munk:

$$\sigma^2 \approx 0.003 + 0.00512U \quad (11)$$

Hu:

$$\sigma^2 = 0.0146\sqrt{U}, (U < 7 \text{ m/s}) \quad (12)$$

$$\sigma^2 = 0.003 + 0.00512U, (7 \leq U < 13.3 \text{ m/s}) \quad (13)$$

$$\sigma^2 = 0.138 \log_{10} U - 0.084, (U \geq 13.3 \text{ m/s}). \quad (14)$$

We used the Gram-Charlier distribution suggested by Cox and Munk (1954) [21] to represent the sea surface slope distribution as did Monahan (2006) [40]. For wind speeds between 7 and 13.3 m s^{-1} , many authors [5, 21, 39] give a linear or a linear-like σ^2 vs U relation. The influence of skewness and kurtosis is small implying that the distribution is close to Gaussian in this wind speed range. Based on the Gram-Charlier distribution we assume that the signal due to surface backscattering for CALIOP is given by:

$$\gamma_U = \frac{\rho}{4\pi\sigma^2 \cos^4 \theta} \exp\left(-\frac{\tan^2 \theta}{\sigma^2}\right)(1 + \Delta(\sigma)) \quad (15)$$

where the slope variance is represented by the Cox-Munk relation: $\sigma^2 = 0.003 + 0.00512U$. Equation 15 represents an one-dimensional Gaussian distribution modified by kurtosis and skewness described by the $\Delta(\sigma)$ term, which can be expressed as the following polynomial in $1/\sigma$ as described below:

$$\Delta(\sigma) = -0.0002\frac{1}{\sigma^4} + 0.0076\frac{1}{\sigma^3} - 0.1008\frac{1}{\sigma^2} + 0.4780\frac{1}{\sigma} - 0.8232. \quad (16)$$

Based on Multiangle Imaging Spectroradiometer (MISR) observations, Shi and Cressie (2007) [41] give a global distribution of the AOD. The southern hemisphere between 23 and 40 degrees in latitude is the cleanest area. The collocated CALIOP and AMSR-E data used in the fitting

analysis is obtained between 23 and 40 degrees in latitude in the southern hemisphere. Compared with the Gaussian distribution, the Gram-Charlier distribution contains a higher order “correction” that depends on the parameter σ (see Appendix). We fitted this correction term ($\Delta(\sigma)$ in Eq. 15) by comparing the residual between the sea surface backscatter observed and estimated from Eq. 15. The fitting is done in powers of $\frac{1}{\sigma}$ (see Eq. 16 and Fig. 4), where the variance σ^2 is a function of wind speed parameterized by Eq. 11.

A comparison of Gaussian and Gram-Charlier distribution is provided in Fig. 5. The comparison is based on the 5-year dataset. In order to minimize the uncertainty from the aerosols, the data located in the region between 23 and 40 degrees in latitude of the Southern hemisphere were selected. The x -axis stands for the surface backscatter observed by CALIOP. The y -axis stands for the modeled surface signal from theory. The y -axis of the left column is based on the Gaussian distribution (Eq. 10), while the right column is based on the Gram-Charlier distribution (Eq. 15) which is equivalent to the simplified 1-D Gaussian distribution modified by the skewness and Kurtosis terms under the 1-D simplification. A comparison of the left column and the right column shows that the Gram-Charlier distribution can improve the coincidence between the surface model and CALIOP observation for both the 532 nm and the 1064 nm channels. The improvement is significant at strong surface signals which occur at small wind speed.

4. Results and discussion

Statistically, an increase in aerosol loading will increase the IAR . Figure 1 shows the relation between the IAR and the AOD. The exact relation between these two quantities is complex and depends on the microphysical properties of the particles. But the results show that the IAR depends statistically on the AOD with a correlation coefficient of 0.51.

Therefore, a threshold of $IAR < 0.15$ is used to select the “clear” cases which contain predominantly small aerosol particles. A quantitative definition of small particles is based on the ECR . Figure 2 shows a histogram distribution of the ECR , an indicator of particle size, which has a theoretical value between 0.06 and 0.09 for a pure molecular atmosphere. The larger the ECR the larger the size of the atmospheric particles, because the scattering cross section of small particles is relatively weak for the 1064 nm wavelength. Thus, as particles increase in size, the numerator of the ECR increases compared to the denominator. From the histogram distribution of the ECR (Fig. 2), we note that there is a normal distribution with a center at 0.22 superimposed on several other normal distributions with centers at higher values. Together Figs. 1 and 2 show that the IAR is also related to the size distribution of the particles. When the IAR is larger than 0.02, the ECR distribution peaks close to 1, while when the IAR is between 0.015 and 0.02, the ECR distribution peaks at 0.6. For IAR values smaller than 0.015, we have the distribution with the smallest peak (0.22). We truncated the dataset and used only the portion with ECR values smaller than 0.40 as the definition of the “clear” sky condition which contains predominantly small size aerosol particles.

Figure 3 shows the global distribution of the truncated ECR . The area with highest ECR values are located off the west coast of Africa and the coast of South America where there is a high generation rate of smoke aerosols. The results show that there are two high value belts. The main one, in the tropical area, is due to strong and frequent convective activity that can prolong the residence time of suspended particles in the atmosphere. The other high ECR belt, located in the southern ocean area, is due to sub-micron sea salt particles generated by strong winds.

The optical depth of the small size aerosol particles which are selected through the IAR and ECR thresholds is shown in Figs. 6 (532 nm channel) and 7 (1064 nm channel). The AOD obtained from the surface reflection is shown in the upper panel and that from the CALIPSO level 2 in the bottom panel. AOD values derived both from our surface AOD method and from CALIPSO level 2 show a “belt” of high values located in the southern 45-55 degree latitude region where there are strong westerly winds. These strong westerly winds generate a significant

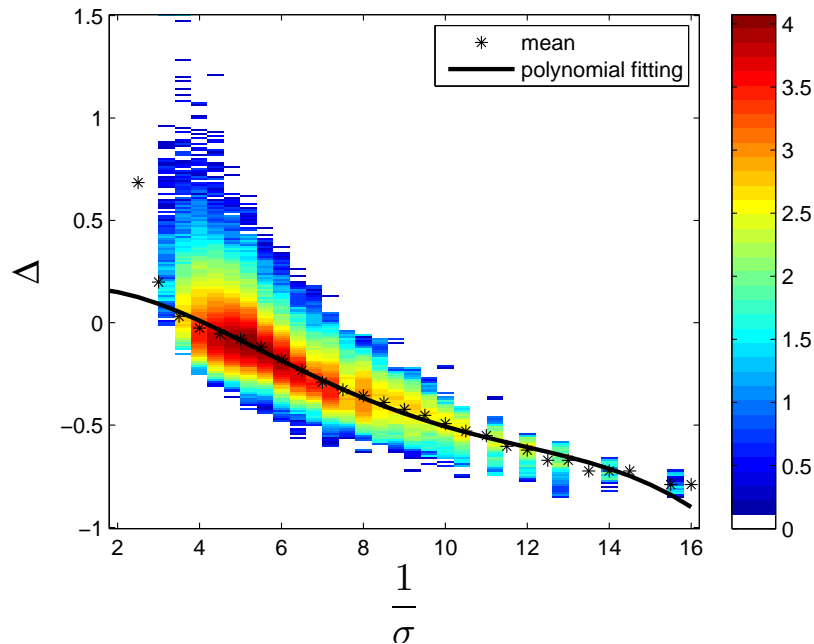


Fig. 4. Behavior of the $\Delta(\sigma)$ term in the Gram-Charlier distribution according to Eq. 16. The x-axis is the inverse of the standard deviation of the slope distribution, and the y-axis is $\Delta(\sigma)$. The observations are represented in colors. The color bar values are the occurrence probability of the observation in absolute numbers in 10^9 .

amount of sea salt particles that are injected into the atmosphere. In the tropical area, the clear sky AOD values derived from the surface method show a more distinct high AOD belt than the AOD values obtained from the CALIPSO level 2 dataset. This belt of high AOD values is due to frequent and strong convective activity in the tropics. The convection can result in large updraft speeds implying that the aerosols can have longer residence times. In extreme cases particles may be injected into the stratosphere, where they may reside for weeks. The clear sky AOD has peak values as high as 0.15 which are comparable in magnitude with AOD values obtained from the CALIPSO level 2 dataset over the West Africa and South Asia coastal areas. However, our surface AOD approach gives AOD values that disagree with the CALIPSO level 2 product in the northern hemisphere. Here, our surface method yields higher AOD values which can be explained by the existence of more aerosol sources in the northern than in the southern hemisphere. The aerosols generated over the continents can be transported to oceanic areas as explained by Huang et al. (2008, 2014) [42, 43].

The case for the 1064 nm channel is shown in Fig. 7. The clear sky AOD values derived from the surface signal have the following spatial distribution: the southern hemisphere has relatively low values and the northern hemisphere relatively high values. This behavior is also explained by the fact that the northern hemisphere has more particles due to transport from the continents. By comparison, in the CALIPSO level 2 dataset the clear sky AOD values in the 1064 nm channel show more asymmetry between the southern and the northern hemispheres.

The strong westerly wind belt which appears in the 532 nm channel in the southern hemisphere is less distinct for the 1064 nm channel. The reason may be that the 1064 nm channel is more sensitive to absorption but less sensitive to scattering by small particles. The main source of absorbing aerosols is black carbon (from combustion processes) and dust particles [6]. Both

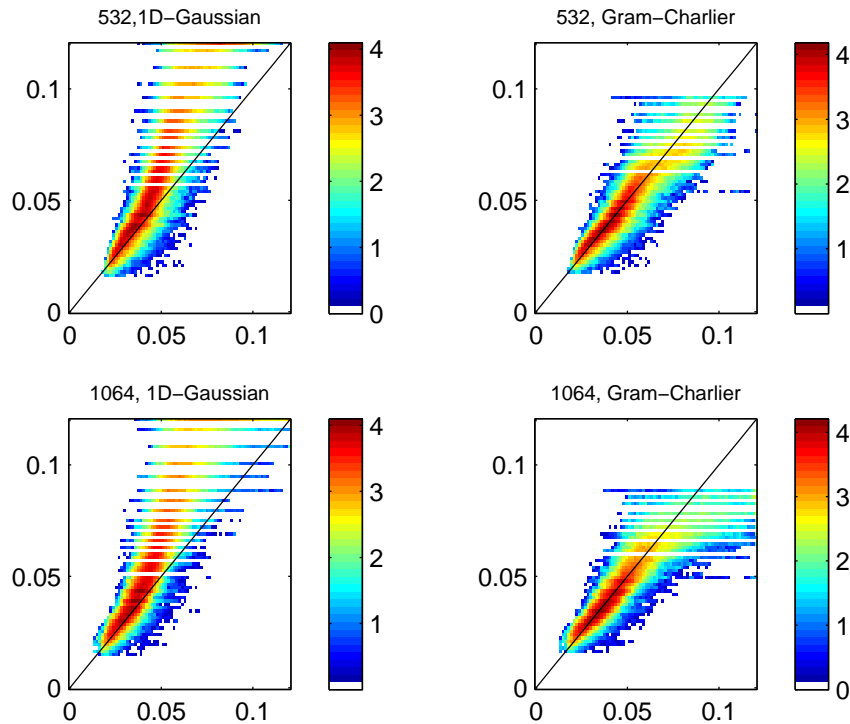


Fig. 5. Scatter plot of the surface backscatter signal. The x -axis is the backscatter deduced from CALIOP observations, and the y -axis is the estimated surface backscatter inferred from theory. The left panels are based on a 1-D Gaussian distribution ($\Delta(\sigma) = 0$). The right panels are based on the Gram-Charlier distribution ($\Delta(\sigma) \neq 0$). The top panels are for the 532 nm channel and the bottom panels are for the 1064 nm channel. The color bar values are the occurrence probability of the observation in absolute numbers in 10^7 .

black carbon and dust particles have higher generation rates in the northern than in the southern hemisphere. Also the 1064 nm signal is not sensitive to the small sea salt particles which have a high generation rate in the strong wind belt of the Southern Ocean.

The clear sky AOD values derived from the surface signal agree with those available from the standard CALIPSO level 2 product in most ocean areas of the southern hemisphere; the difference between them is smaller than 0.015. But the surface derived clear sky AOD values are higher than those obtained from the standard CALIPSO level 2 product in the rest of the ocean areas. The greatest difference between them is found in the tropical area and the coastal areas of south Asia with differences ranging from 0.04 to 0.06.

Uncertainties in AOD values derived from the surface method stems from the sea surface reflection model and the calibration. The standard deviation (std) of the “clear” sky AOD values derived from the surface method is shown in Fig. 8 The average std is 0.03. The global distribution of the std is relatively uniform. This uniform distribution suggests that the calibration is not the main source of uncertainty, because the calibration of CALIOP depends on latitude due to the latitude-dependent thermal status of the satellite.

The following issues may introduce uncertainties associated with the surface method. First, there is a small likelihood that CALIOP may become saturated on single shot resolution when

wind speed is very low (e.g., less than 1 m/s). Although we carefully remove profiles that may potentially be saturated, by doing so we may introduce bias in aerosol statistics. Secondly, at CALIOP's 30 m vertical resolution, the surface backscatter from highly productive waters can be contaminated by phytoplankton backscatter and be effected by surfactants. Our future studies will try to address these issues.

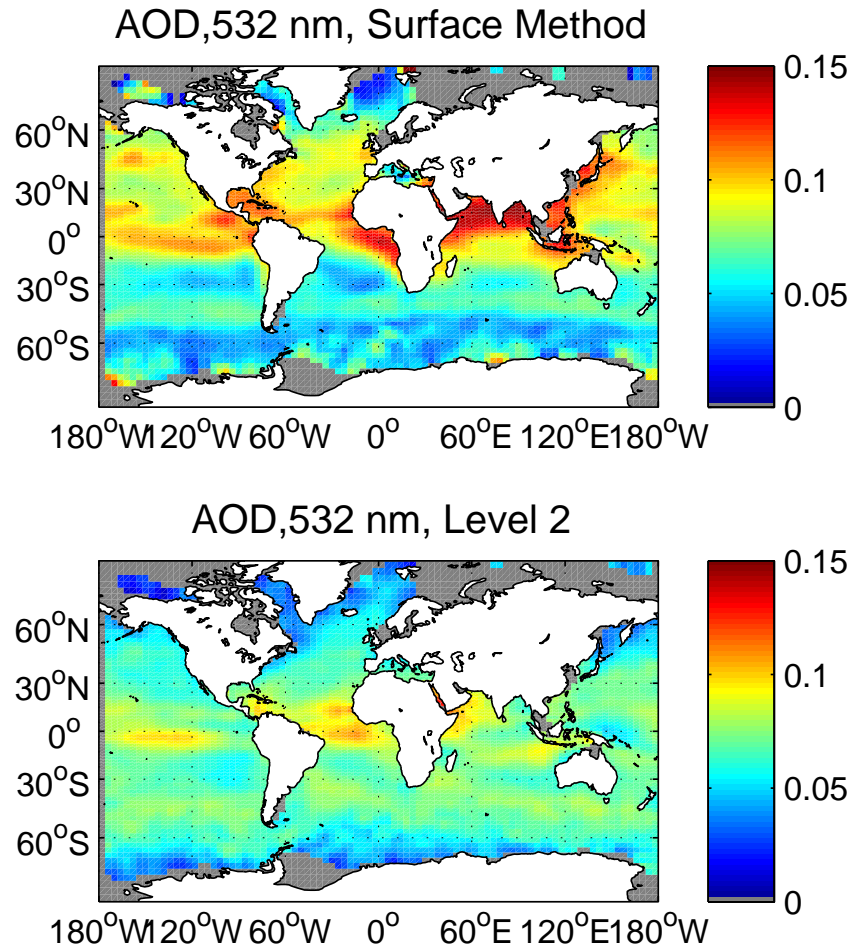


Fig. 6. Global distribution of the clear sky AOD distribution for the 532 nm channel. The color represents the AOD value. Top panel: the AOD based on the surface signal according to Eq. 7. Bottom panel: AOD obtained from the CALIPSO level 2 product. The average is made on a 2° (latitude) by 4° (in longitude) grid box over the 5-year dataset.

5. Conclusions

The goal of this paper was to get an observation-based estimation of the AOD for “clear” sky conditions for the purpose of atmospheric correction of satellite observations over the ocean. A five year collocated CALIPSO and AMSR-E dataset was used to analyze the clear sky AOD.

The “clear” sky condition is defined such that CALIOP has an Integrated Atmosphere Return

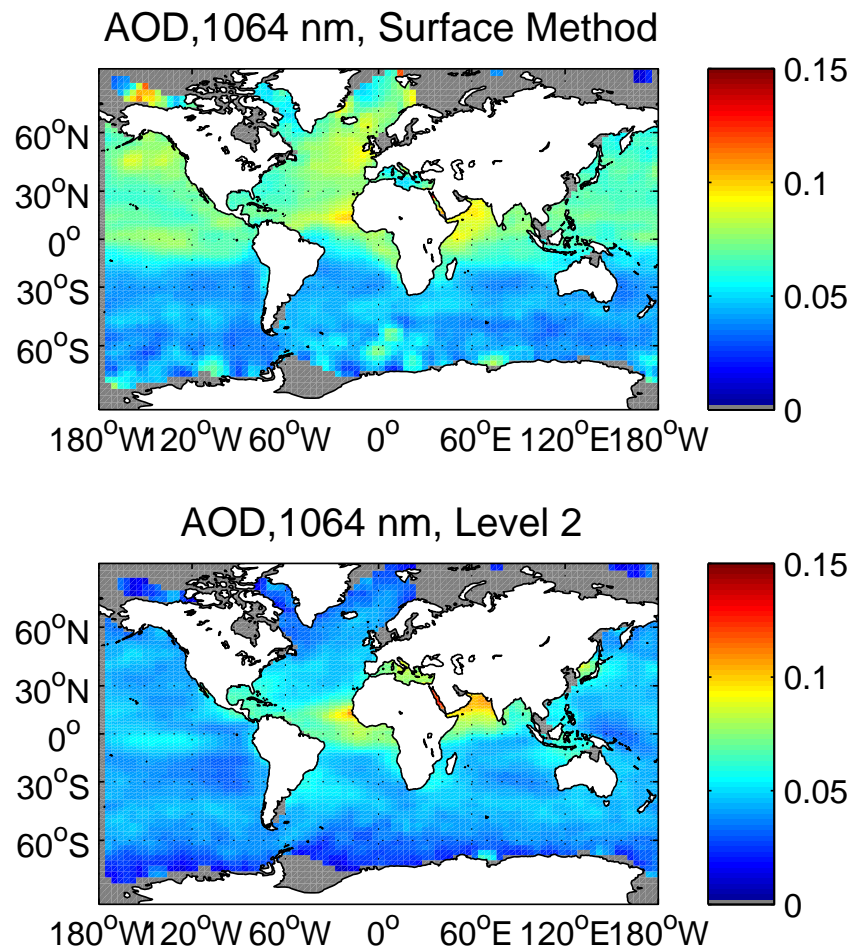


Fig. 7. Global distribution of the clear sky AOD distribution for the 1064 nm channel. The color represents the AOD value. Top panel: the AOD based on the surface signal according to Eq. 8. Bottom panel: AOD obtained from the CALIPSO level 2 product. The average is made on a 2° (latitude) by 4° (in longitude) grid box over the 5-year dataset.

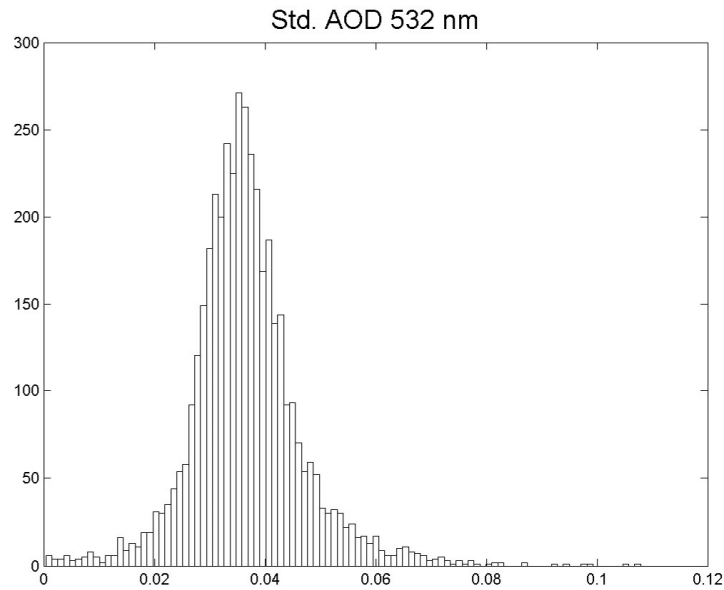


Fig. 8. The histogram distribution of the Standard Deviation (Std.) of the clear AOD from surface method at the 532 nm channel. The Std. is calculated on each grid box of the global distribution.

(*IAR*) less than 0.015 and a small value of the Equivalent Color Ratio (*ECR*). Molecules and aerosol particles have different *ECR* values. The *ECR* also increases with particle size. Thus, we can identify cases with sufficiently small but optically-significant particles. Although we cannot get an accurate estimate of the exact size of the particles, most likely they have sizes in the 0.1–1 μm range.

The global distribution of the *ECR* has two belts with high values. The main one is located in the tropics and the secondary belt is located in the Southern Ocean. These areas are characterized by high frequency of convective activity and high generation of sea salt aerosols, respectively. The *ECR* is related to the aerosol residence time and the aerosol generation rate.

The sub-micron sea salt aerosols in the strong westerly wind belt are identified by both the surface method and in the CALIPSO level 2 data. The AOD due to small particles derived by the surface method is much larger than that of the CALIPSO level 2 aerosol product in the tropics and the coast of south Asia since the AOD derived from the surface method contains the effects of absorption and multiple scattering. The most significant difference between the AOD derived from surface method and the AOD in the CALIPSO level 2 product is found in the northern hemisphere which contains aerosols transported from the continents. This transported aerosol component contains dust aerosol from the eurasian continent.

The small particles have weaker scattering at 1064 nm than at 532 nm. The surface signal derived clear sky AOD in the 1064 nm channel is more sensitive to absorbing aerosols which are mainly black carbon and dust particles. The source of the black carbon aerosol is due to combustion processes while the source of the dust aerosol is transport from the continents. These two types of aerosol particles are more abundant in the northern than in the southern hemisphere.

The average uncertainty of the AOD derived by the surface method is 0.03 in the 532 nm channel. However, the global distribution of the uncertainty is quite uniform. In principle, the accuracy of the clear sky AOD derived by the surface method depends on the surface reflection

model and the instrument calibration. Because the calibration is latitude dependent and the uncertainty appears to be quite uniform, we conclude that the uncertainty stems mainly from the surface reflection model.

6. Appendix

We assume that the surface slopes obey the Gram Charlier distribution proposed by Cox and Munk [21]:

$$P(z_x, z_y) = \frac{1}{2\pi\sigma_x\sigma_y} \exp\left[-\frac{1}{2}\left(\frac{z_x^2}{\sigma_x^2} + \frac{z_y^2}{\sigma_y^2}\right)\right] \left\{1 - \frac{1}{2}C_{21}(\xi^2 - 1) - \frac{1}{6}C_{03}(\eta^3 - 3\eta) + \frac{1}{24}C_{40}(\xi^4 - 6\xi^2 + 3) + \frac{1}{4}C_{22}(\xi^2 - 1)(\eta^2 - 1) + \frac{1}{24}C_{04}(\eta^4 - 6\eta^2 + 3)\right\}$$

where C_{21} and C_{03} are skewness coefficients, C_{40} , C_{22} and C_{04} are kurtosis (peakedness) coefficients, and $\sigma_{x,y}$ are rms values of the surface slope component in the x and y directions. $\xi = z_x/\sigma_x$ and $\eta = z_y/\sigma_y$ are the ratio of the slope to the standard deviation of the distribution for the x and y components, respectively. In the absence of skewness ($C_{21} = C_{03} = 0$), and peakedness ($C_{40} = C_{22} = C_{04} = 0$) the Gram-Charlier series reduces to a two-dimensional Gaussian

$$P(z_x, z_y) = \frac{1}{2\pi\sigma_x\sigma_y} \exp\left[-\frac{1}{2}\left(\frac{z_x^2}{\sigma_x^2} + \frac{z_y^2}{\sigma_y^2}\right)\right]. \quad (17)$$

For an isotropic slope distribution, $\xi = \eta$ (no directional dependence), the distribution becomes a one-dimensional Gaussian modified by skewness and kurtosis effects:

$$P(\tan \theta) = \frac{1}{\pi\sigma^2} \exp\left[-\frac{\tan^2 \theta}{\sigma^2}\right] (1 + \Delta(\sigma)) \quad (18)$$

where $\Delta(1/\sigma) = \sum_{i=0}^4 C_i \sigma^i$. For CALIPSO observations, only local facets with slopes equal to the fixed CALIPSO observation zenith angle can reflect light into the CALIOP receiver.

Cox and Munk [21] parameterized the skewness and kurtosis in terms of the wind speed using a statistical method that led to uncertainties in the coefficients of the same (or even higher) order of magnitude as the coefficients themselves. We used the collocated CALIPSO and AMSR-E data set to parameterize the higher order terms $\Delta(\sigma)$ of the Gram-Charlier distribution. However, due to the very limited observation angles of CALIPSO, we cannot distinguish between skewness and kurtosis effects.

Acknowledgments

The data used in this paper were obtained from the NASA Langley Research Center Atmospheric Science Data Center.